Luminescence of Triple Perovskite Ba₃MgTa₂O₉:Dy³⁺ Up to 1100 °C

Marcos R. Imer, Amos Afugu, Zhen-Fei Liu, and Federico A. Rabuffetti*

Department of Chemistry, Wayne State University, Detroit, MI 48202, USA

*Corresponding Author. Email: far@chem.wayne.edu

ABSTRACT

The luminescence response of Dy³⁺-doped Ba₃MgTa₂O₉ (BMTO:Dy) between room temperature and 1100 °C was studied in the context of high-temperature thermosensitive phosphors. Singlephase BMTO:Dy was synthesized via solid-state reaction. Powder X-ray diffraction, diffuse reflectance spectroscopy, and density-functional theory calculations were used to probe its crystal and electronic structure. Variable-temperature time-resolved decays of the ${}^4I_{15/2} \rightarrow {}^6H_{15/2}$ transition of Dv3+ (457 nm) were collected and the temperature dependence of the excited state average lifetime was quantitatively analyzed with two objectives: establish mechanisms driving luminescence thermal quenching and assess the potential of BMTO:Dy as a high-temperature luminescent thermometer. Quenching was observed above 450 °C and appeared to be driven by thermal ionization of the Dy^{3+ 4}I_{15/2} excited state to the host's conduction band, with a temperaturedependent activation barrier in the 1.1–1.5 eV range. The occurrence of high-order (≈21) multiphonon relaxation to lower-lying 4f levels as an additional or alternative quenching pathway at high temperatures could not be ruled out. As a luminescent thermometer, the operational temperature range of BMTO:Dy was between 450 and 1100 °C and temperature sensitivities ranged between ≈2.1 % °C⁻¹ at 538 °C and ≈0.9 % °C⁻¹ at 1100 °C. Findings presented herein expand the library of high-temperature thermosensitive phosphors to group V d⁰ refractory metalates, a class of materials that offers the opportunity to tailor luminescence response through rational tuning of phosphor's crystal, vibrational, and electronic structure.

INTRODUCTION

Thermosensitive phosphors are ideal temperature sensors for combustion applications, where temperatures typically exceed 500 °C. Their unique suitability is predicated on their ability to operate in environments where contact thermometry and pyrometry are problematic to implement and do not afford adequate performance in terms of temperature accuracy and spatial resolution.¹⁻⁴ The ability of thermosensitive phosphors to serve as thermal markers in combustion systems is illustrated by a number of examples that encompass both basic and applied materials research problems. Included in that list are understanding failure mechanisms and predicting lifetimes of thermal barrier coatings in gas turbine engines,⁵⁻⁷ surface temperature mapping and establishing the dynamics of heat flow in combustors, 8-21 mapping temperature fields in hot gas flows, ^{22, 23} and in-service monitoring of rotating components in turbomachinery. ¹⁸ Thermosensitive phosphors typically consist of a host matrix doped with an activator. Temperature sensing may be approached from a lifetime or a ratiometric standpoint, the former being preferred for high-temperature combustion applications. In this approach, the lifetime of the activator's emissive state (τ) serves as the thermometric parameter to convert optical signals to temperature values. Lifetime depends on the rates of radiative and nonradiative relaxation processes, the latter being strongly temperature-dependent and driving luminescence thermal quenching. The rate of change of lifetime with temperature determines the performance of the phosphor as a thermometer. It directly impacts figures-of-merit such as operational temperature range, temperature sensitivity and resolution, and spatial resolution, among others. For example, enhancing thermal quenching leads to a steeper decrease of lifetime, thereby improving temperature sensitivity. From a chemist's perspective, it follows that achieving synthetic control over nonradiative relaxation processes governing thermal quenching is critical to design thermosensitive phosphors with targeted performance.

Exercising synthetic control over thermal quenching pathways requires materials platforms in which structural (topology of cationic substructure), vibrational (phonon frequencies), and electronic features (bandgap) of the host may be compositionally tuned, as these are directly relevant for the luminescence response of the activator. The library of high-temperature thermosensitive phosphors for which experimental luminescence data above 500 °C are available^{8-10, 15-21, 23-57} is largely dominated by Dy³⁺ as the activator of choice (see Supporting Information, **Tables S1** and **S2**). A Dieke diagram of the 4*f* levels of Dy³⁺ is depicted in **Figure 1**, along with

relevant radiative and nonradiative processes. The lifetime of the ${}^4I_{15/2}$ excited state extracted from its decay to the ⁶H_{15/2} ground state is used as the thermometric parameter. The fact that it occurs in the blue region of the spectrum (\$\approx 455 nm) affords minimal interference from blackbody radiation. High-temperature thermosensitive phosphors have been realized by incorporating Dy³⁺ into a number of wide bandgap hosts ($E_g > 6$ eV) including yttria-stabilized zirconia (YSZ = $Y_x Zr_{1-}$ ⁵⁷ silicates (Y₂SiO₅, Y₂Si₂O₇),^{35, 48, 50} and aluminosilicates (Ca₂Al₂SiO₇, (Ba,Sr)Al₂Si₂O₈).^{35, 50} In these hosts, luminescence quenching at high temperatures occurs via high-order multiphonon relaxation (MPR), a process driven by low effective frequency phonons that bridge the gap between the lanthanide's emissive level and lower lying levels. ^{37, 56, 58, 59} This process has been invoked to rationalize quenching in YSZ:Dy above 450 °C (order 18), 10 and Y₃Al₅O₁₂:Dy above 900 °C (order 20)⁵² and 1200 °C (order 23).¹⁰ A remarkable absence in the list of high-temperature phosphors is that of groups V and VI d^0 oxides featuring MO_n^{m-} oxoanions as building blocks, specifically niobates, tantalates, molybdates, and tungstates. These metalates offer a high degree of structural, vibrational, and electronic tunability via chemical substitutions, which is highly desirable from the standpoint of manipulating nonradiative processes governing luminescence thermal quenching.

Triple perovskite Ba₃MgTa₂O₉ (BMTO) serves to illustrate their potential as host materials for high-temperature phosphors on account of its thermal stability and compositional tunability. It has a melting point of 3100 °C and has been examined as a candidate for thermal coatings. $^{60-62}$ Its crystal structure is shown in **Figure 2** and is amenable to a wide range of chemical substitutions. BMTO crystallizes in the $P\overline{3}m1$ hexagonal space group and exhibits the archetypical perovskite arrangement (**Figure 2a**). 63 Barium sits in cuboctahedral holes in the A site, while corner-sharing MgO₆ and TaO₆ octahedra are located in the B site. Ba²⁺ ions occupy two distinct holes, which differ from each other in the second coordination shell of barium, specifically in the number of neighboring Mg²⁺ and Ta⁵⁺ ions (**Figure 2b**). Aliovalent substitutions include lanthanide doping in the A site of the perovskite lattice 64 and may be performed to impart luminescence response. Isovalent substitutions in the A and B sites 63 , 65 , 66 may be conducted to tune metal connectivity, vibrational frequencies, and bandgap. BMTO features an indirect bandgap of \approx 4.3 eV, 67 significantly narrower than that of hosts typically used in high-temperature phosphors (vide supra). This feature is noteworthy because it may open an alternative luminescence quenching pathway

via thermally activated charge transfer (CT) from the activator's excited state to the host conduction band (CB).⁶⁸ Thermal ionization of excited Dy³⁺ to the conduction band has been proposed as the primary quenching mechanism for group V metalate phosphors GdVO₄:Dy⁶⁹ (E_g = 3.9 eV)⁷⁰ and LiNbO₃:Dy⁷¹ (E_g = 3.7 eV)⁷². In spite of their potential, lanthanide-doped BMTO and substituted derivatives have not been studied as high-temperature thermosensitive phosphors.

In this article we report an investigation of the luminescence response of Dy³⁺-doped Ba₃MgTa₂O₉ (BMTO:Dy) from room temperature to 1100 °C. Single-phase BMTO:Dy was synthesized via solid-state reaction and variable-temperature time-resolved decays of the ${}^4I_{15/2} \rightarrow {}^6H_{15/2}$ transition of Dy³⁺ were collected using a custom-made furnace with optical access ports. Luminescence decays were quantitatively analyzed with the aim of establishing thermal quenching pathways. To this end, the location of the 4f levels of Dy³⁺ within the bandgap of the BMTO host was estimated, a task that was aided by diffuse reflectance spectroscopy and electronic structure calculations. Finally, the potential of BMTO:Dy as a high-temperature luminescent thermometer was assessed from the standpoint of its operational temperature range and temperature sensitivity.

EXPERIMENTAL

Synthesis of Dy^{3+} -doped $Ba_3MgTa_2O_9$. ≈ 1 g of polycrystalline Dy^{3+} -doped $Ba_3MgTa_2O_9$ (BMTO:Dy) was synthesized via solid-state reaction. Aliovalent substitution of Dy^{3+} for Ba^{2+} was performed according to the chemical formula $Ba_{3-3x}Dy_{3x}Mg_{1+x}Ta_{2-x}O_9$, which was previously employed to dope La^{3+} into BMTO.⁶⁴ Our target composition was $Ba_{2.97}Dy_{0.03}Mg_{1.01}Ta_{1.99}O_9$, corresponding to a doping level of 1 mol. %. We deliberately chose a low doping level to minimize the likelihood of energy transfer between Dy^{3+} centers.⁶⁸ $BaCO_3$ (99.98%), Dy_2O_3 (99.99%), MgO(99.99%), and Ta_2O_5 (99.99%) from Sigma-Aldrich were used as reagents. All were used as received. Stoichiometric amounts of the starting materials were mixed and ground in an agate mortar. The unreacted mixture was placed in an alumina crucible and heated at 1300 °C for 108 h under air. Intermediate grindings were performed every 12 h. Heating and cooling rates of 5 and 20 °C min⁻¹ were employed, respectively. A solid white powder was obtained. Pellets for high-temperature luminescence studies were prepared by mixing ≈ 1 g of BMTO:Dy with isopropyl alcohol, drying the mixture for 2 h, and pressing it under 6 tons for 15 min. The resulting pellets (13 mm diameter, 2 mm thick) were annealed at 1000 °C for 12 h under air.

Powder X-ray Diffraction (PXRD). PXRD patterns of BMTO:Dy were collected using a Bruker D2 Phaser diffractometer operated at 30 kV and 10 mA. Cu Kα radiation ($\lambda = 1.5418$ Å) was employed. A nickel filter was used to remove Kβ. Diffractograms were collected in the $10-110^{\circ}$ 2θ range using a step size of 0.02° and a step time of 0.5 s.

Rietveld Analysis. Rietveld analysis of PXRD data was performed using the General Structure Analysis System II (GSAS-II). The Following Parameters were refined: (1) scale factor; (2) background, which was modeled using a Chebyshev function; (3) instrument parameters, including diffractometer constant and contributions to peak profile; (4) lattice constants; (5) atomic coordinates when allowed by symmetry; (6) three isotropic atomic displacement parameters ($U_{Ba,Dy}^{iso}$, $U_{Mg,Ta}^{iso}$, U_{O}^{iso}); and (7) crystallite size and microstrain. Site occupancies (f) were set according to the chemical formula $Ba_{2.97}Dy_{0.03}Mg_{1.01}Ta_{1.99}O_9$. For all barium sites these were fixed to $f_{Dy} = 0.01$ and $f_{Ba} = 0.99$. In the case of Mg^{2+} and Ta^{5+} sites, occupancies were fixed to $f_{Mg} = 0.99$ and $f_{Ta} = 0.01$ in the Mg1/Ta1 site, and $f_{Mg} = 0.01$ and $f_{Ta} = 0.99$ in the Ta2/Mg2 site. Difference curve and $T_{Ab} = 0.99$ in the refined structural model, which was visualized using VESTA. The

UV-visible Diffuse Reflectance. Reflectance spectra were collected between 200 and 800 nm using a Jasco V570 UV-vis-NIR spectrophotometer featuring a 60 mm integrating sphere. BaSO₄ (99.99%, Sigma-Aldrich) was used as a reflectance standard. Reflectance (R) was converted to absorbance using the Kubelka-Munk function F(R), $F(R) = (1 - R)^2/2R$.

Electronic Structure Calculations. First-principles density-functional theory (DFT) was employed to compute the band structure and projected density of states (PDOS) of BMTO. Starting from the crystal structure obtained from Rietveld analysis of PXRD data, lattice parameters and atomic positions were optimized using a kinetic energy cutoff of 70 Ry, a $6 \times 6 \times 5$ *k*-mesh, the projector augmented wave method,⁷⁸ and the Perdew–Burke–Ernzerhof (PBE)⁷⁹ functional as implemented in the Quantum ESPRESSO⁸⁰ package. The structure was considered fully relaxed when all residual forces were below 0.05 eV/Å. Optimized lattice parameters equaled a = 5.837 Å and c = 7.167 Å, both within 1% of the experimental values. After computing band structure and PDOS using the PBE functional, we employed the Heyd–Scuseria–Ernzerhof (HSE)⁸¹ hybrid functional to obtain a more quantitatively accurate picture of the frontier band energies and

bandgap. The HSE calculation was performed using a $2 \times 2 \times 2$ k-mesh to reduce the computational cost; at the PBE level, a $2 \times 2 \times 2$ k-mesh only leads to a 0.01 eV/atom total energy difference compared to the $6 \times 6 \times 5$ k-mesh.

Room-Temperature Luminescence. Photoluminescence analyses were conducted using a Fluorolog 3–222 (Horiba Scientific). Steady-state excitation and emission spectra were collected using a 450 W xenon lamp as the excitation source and a photomultiplier tube (PMT) R928 as the detector. Time-resolved decays were recorded using a 262 nm Q-switched laser as the excitation source (QL262-020, CrystaLaser, 15 uJ per pulse at 1 KHz, 12 ns pulse length). Slit widths equal to 1.5 and 10 nm were used to acquire steady-state and time-resolved data, respectively.

Variable-Temperature Luminescence. (i) Instrumentation. As shown in Figure 3, a furnace with optical access ports was built in house to probe the luminescence response of BMTO:Dy at high temperatures. The furnace consisted of a 2.54 cm diameter spiral microheater (MC-AM-1-30, Micropyretics Heaters International Inc.) and a ceramic insulation box with dimensions 22 × 16.5×16.5 cm ($w \times h \times d$, see **Figure 3a**). The microheater was embedded in a ceramic brick (11 \times 6.5 \times 2 cm) positioned 5 cm above the bottom of the insulation box. The heating element was powered by a DC power supply (CSI3030SW, Circuit Specialists) and its temperature was controlled through a closed loop involving an N-type thermocouple (TJ36-NNXL-14E-12, Omega Engineering Inc.) and a PID controller (E5AC, Omron Corp.). The thermocouple, labeled T2 hereafter, was placed ≈0.5 mm above an alumina disk (1.3 cm diameter, 2 mm thick) on top of which the phosphor pellet sat. The disk, in turn, was positioned ≈2 mm above the heating coil of the microheater. A second N-type thermocouple labeled T1 was placed ≈2.2 cm across from T2 to provide an additional temperature reading and estimate the thermal gradient across the pellet (**Figure 3b**). Temperature readings from both thermocouples (T_{T1} and T_{T2}) were recorded in real time and stored using a handheld calibrator thermometer connected to a computer (CL3515R, Omega Engineering Inc.). The dimensions of the furnace cavity were $4 \times 3 \times 4.5$ cm. Two optical access ports were drilled through the ceramic insulation, one for excitation of the phosphor pellet and one for collection of emitted photons. Excitation was carried out normal to the pellet surface using a 262 nm Q-switched laser (vide supra). A short-pass UV filter (FF01-300/SP-25, Semrock) and a cylindrical plano-convex lens (LJ4667RM, Thorlabs Inc.) were placed along the laser beam path. Photoluminescence emission was collected at 30° using a custom-made optic fiber (Photran LLC). This probe consisted of a ≈25 cm long unclad sapphire optic fiber (450 µm core diameter)

within a stainless-steel sleeve. The fiber extended ≈ 5 mm beyond the distal end of the sleeve and its tip was positioned ≈ 5 mm above the pellet surface (**Figure 3c**). Photons collected by this fiber were directed to the entrance of the emission monochromator of the Fluorolog 3–222 via a silica fiber (FG550LEC, Thorlabs Inc.). The R928 PMT of the fluorometer served as the detector. Phosphor excitation and photon detection were synchronized via connection of the laser and PMT to the data acquisition hardware. Output signals were processed into time-resolved decays using data acquisition software. Two different combinations of acquisition hardware and software were employed depending on the timescale of the luminescence decay. Multichannel scaling (MCS) was used to count photons arising from slow decays ($\tau > 10~\mu s$). This was accomplished by coupling the laser and the PMT to the DeltaHub module of the fluorometer and using DataStation (Horiba Scientific) for data acquisition (i.e., triggering the laser and recording PMT output). Time correlated single photon counting (TCSPC) was the method of choice to collect faster decays. TCSPC was accomplished by connecting the laser and PMT to a digital oscilloscope (PCI-5154, National Instruments Corp.) and using a LabVIEW code written in house for data acquisition (see Acknowledgements).

(ii) Collection of Variable-Temperature Time-Resolved Decays. Luminescence decays were recorded at room temperature and between 100 and 1100 °C in 100 °C increments. The phosphor pellet was heated to the target temperature (T_{Target}) at a rate of ≈ 10 °C min⁻¹. Once readings in both thermocouples stabilized within a window of 1 °C or less, the pellet was allowed to dwell for 15 min prior to data collection. The decay of the ${}^4I_{15/2} \rightarrow {}^6H_{15/2}$ emission of Dy³⁺ was monitored at 457 nm. Monochromator entrance slit width was set equal to 10 nm. Decays were collected using MCS from room temperature to 600 °C (repetition rate ranging from 45 to 630 Hz) and TCSPC between 700 and 1100 °C (repetition rate fixed at 1 KHz). The instrument response function (IRF) was recorded using colloidal silica as the scattering medium (Ludox, Sigma-Aldrich) and the digital oscilloscope as the acquisition hardware. The laser repetition rate was set to 1 KHz.

RESULTS AND DISCUSSION

The phase purity and bandgap of polycrystalline BMTO:Dy were examined prior to investigating its luminescence response. We sought to probe incorporation of Dy³⁺ into the perovskite host lattice and obtain a reliable estimation of its bandgap, which we expected to be instrumental in rationalizing thermal quenching pathways. Results from these studies are

summarized in Figure 4. Rietveld analysis of PXRD data demonstrated the phase purity of BMTO:Dy. All diffraction maxima were indexed to the BMTO structure (PDF No. 01–073–4184); no secondary crystalline phases were observed (Figure 4a). Crystallochemically meaningful structural parameters were extracted from the refinement (see Supporting Information, **Table S4**). Altogether, these results supported incorporation of 1 mol. % of Dy³⁺ into the perovskite host. The thermal stability of the phosphor was confirmed using thermogravimetric and differential thermal analysis (see Supporting Information, Figure S1). Neither a weight loss nor phase transitions were observed upon heating the phosphor to 1200 °C under air. Further, diffraction patterns collected before and after thermal analysis were identical. The bandgap of the phosphor was examined experimentally using UV-vis diffuse reflectance spectroscopy, and theoretically via DFT. Reflectance spectra of pristine and doped BMTO were collected and the onsets of the absorption edges were used to estimate the bandgap, yielding $E_g \approx 4.60$ eV in both cases (**Figure 4b**). Pristine BMTO was prepared following the same synthetic procedure used for its doped counterpart. Bandgaps estimated herein were wider than most of those reported on the basis of experimental measurements (3.90, 3.93, and 4.28 eV)^{67, 82, 83} and theoretical calculations (3.49 and 3.27–3.92 eV)84,85. In view of this discrepancy, we decided to carry out a theoretical investigation of the electronic structure of BMTO. The band structure computed using the PBE functional showed that this perovskite is an indirect bandgap semiconductor in which the valence band (VB) maximum and conduction band (CB) minimum are located at A and Γ points, respectively (Figure 4c). Calculations using the experimentally determined structure yielded very similar results to the fully relaxed structure (**Table S5**). The PDOS revealed that the top of the VB is dominated by the 2p orbitals of oxygen, whereas the 5d orbitals of tantalum are the major contributors to the bottom of the CB (Figure 4c, Figure S2). Thus, optical absorption in BMTO entails O²⁻ to Ta⁵⁺ charge transfer. The HSE functional yielded an indirect A $\rightarrow \Gamma$ bandgap of 4.58 eV. This value is in excellent agreement with our experimental estimate and with that reported by Borlido and coworkers on the basis of pseudopotential calculations using the modified Becke-Johnson functional (4.56-4.58 eV).85

The photoluminescence response of BMTO:Dy was first screened at room temperature to pinpoint suitable excitation and emission wavelengths for collection of variable-temperature time-resolved decays. Results from these studies are summarized in **Figure 5**. The excitation spectrum monitored at 589 nm (${}^4F_{9/2} \rightarrow {}^6H_{13/2}$ transition of Dy³⁺) was dominated by a broad band peaking

at ≈ 260 nm (4.77 eV), corresponding to bandgap absorption (O^{2-} to Ta^{5+} charge transfer) and subsequent energy transfer to Dy^{3+} (**Figure 5a**). Excitation of Dy^{3+} via 4f—4f transitions led to much weaker emission (see inset of **Figure 5a**). On this basis, the emission spectrum of the phosphor was collected using 260 nm as the excitation wavelength. The spectrum featured the usual bands arising from radiative relaxation of the ${}^4I_{15/2}$ and ${}^4F_{9/2}$ levels to the 6H_1 manifold. Although weak at room temperature, emission arising from the temperature-sensitive ${}^4I_{15/2} \rightarrow {}^6H_{15/2}$ transition was observed at 457 nm. The time-resolved decay of this transition was collected under 262 nm excitation. Fits of the multiexponential function given in **equation 1** were carried out. Here I(t) is the luminescence intensity at time t, t is the number of exponential functions, t is the lifetime of t-th excited state, and t and t are constants. Fractional contributions t were computed according to **equation 2** and the intensity-weighted average lifetime t estimated using **equation 3**. The best fit to the experimental decay was obtained using a

$$I(t) = \sum_{i} A_{i} \exp\left(-\frac{t}{\tau_{i}}\right) + A \tag{1}$$

$$F_i = \frac{\tau_i A_i}{\sum_i \tau_i A_i} \tag{2}$$

$$\langle \tau \rangle = \frac{\sum_{i} \tau_{i}^{2} A_{i}}{\sum_{i} \tau_{i} A_{i}} \tag{3}$$

triexponential function with lifetimes equal to 1429, 473, and 28 μs and fractional contributions equal to 72, 24, and 4 %, respectively (**Figure 5b**). The estimated average lifetime was 1147 μs. A triexponential decay was also reported for BMTO:Eu at doping levels as low as 0.3 mol. %.⁸⁶ We attribute this observation to a multisite distribution of Dy³⁺ activators rather than to energy transfer between them. Multisite distribution likely results from Dy³⁺ replacing Ba²⁺ at two distinct crystallographic sites, and from the presence of nearby oxygen defects that may create an additional subset of emitters.

Characterization of the high-temperature luminescence response of BMTO:Dy entailed two tasks. First, we collected time-resolved decays between room temperature and 1100 °C and fit them to extract Dy³⁺ excited-state lifetimes. Next, we quantitatively analyzed their temperature dependence to rationalize thermal quenching pathways. Experimental decays and fits are shown in **Figure 6**. Fitting windows and fit parameters (τ_i and F_i) are given in **Table 1**, which also

includes temperature readings from the two thermocouples (T_{T1} and T_{T2}), average temperature ($\langle T \rangle$), and average lifetime ($\langle \tau \rangle$). Decays collected in the 22–600 °C (700–900 °C) temperature range were fit between the first (second) data point following the laser pulse and the return of the signal to the baseline. Decays collected at 1000 and 1100 °C were fit by reconvoluting them with the instrument response function; in both cases the start of the fitting window was placed before the edge of the laser pulse. Similar lifetimes were extracted using an intensity threshold^{15, 42, 49, 56} to define the fitting window (see Supporting Information, **Figure S3** and **Table S6**). This approach, however, led to a slight overestimation of lifetimes at 1000 and 1100 °C, where the first point of the decay could not be accurately pinpointed. Inspection of **Table 1** shows that average lifetimes spanned 5 orders of magnitude, from a millisecond at room temperature (1.03 ms) to tens of nanoseconds at 1100 °C (23 ns). The onset of luminescence quenching was clearly noticeable between 400 and 500 °C, where $\langle \tau \rangle$ departed from the nearly constant value associated with radiative relaxation and a ≈4-fold drop in $\langle \tau \rangle$ occurred. Decays showed triexponential behavior up to 600 °C, biexponential between 700 and 900 °C, and monoexponential at 1000 and 1100 °C, indicating the progressive thermal quenching of different subsets of Dy³+ emitters.

The temperature dependence of the average lifetime of Dy³⁺ excited state ${}^4I_{15/2}$ was quantitatively analyzed to establish thermal quenching pathways. The general expression of this dependence is given in **equation 4**, where K_R and K_{NR} are the rates of radiative

$$\tau(T) = [K_{\rm R} + K_{\rm NR}(T)]^{-1} \tag{4}$$

and nonradiative relaxation, respectively. K_R is usually assumed to be temperature-independent, while the functional form of $K_{NR}(T)$ depends on the thermal quenching mechanism. Two quenching pathways were considered for BMTO:Dy; these were multiphonon relaxation of the ⁴I_{15/2} excited state to the lower-lying ⁶F_{1/2} state, and thermally activated charge transfer from the excited state to the host's conduction band. The temperature dependence of the multiphonon relaxation rate (K_{MPR}) is given in equation 5, where $K_{MPR}(0)$ is the spontaneous phonon emission rate, ΔE_{MPR} is the energy gap between the initial and final states,

$$K_{\text{MPR}}(T) = K_{\text{MPR}}(0) \left[1 - \exp\left(-\frac{\Delta E_{\text{MPR}}}{p k_B T}\right) \right]^{-p}$$
 (5)

p is the number of phonons needed to bridge that gap, k_B is Boltzmann's constant, and T is the absolute temperature. ⁸⁷⁻⁹⁰ In the case of nonradiative relaxation via charge transfer to the CB, two distinct models may be invoked to quantitatively explain the time evolution of 4f excited states as a function of temperature. A single-barrier Mott–Seitz model—hereafter referred to as charge-transfer model (CT)—is the simplest of these two alternatives. ^{68,91-93} In this model the temperature dependence of the charge transfer rate ($K_{\rm CT}$) is given by an Arrhenius-type expression shown in **equation 6**, where $C_{\rm CT}$ is a frequency factor and $\Delta E_{\rm CT}$ is the energy difference between

$$K_{\rm CT}(T) = C_{\rm CT} \exp\left(-\frac{\Delta E_{\rm CT}}{k_B T}\right)$$
 (6)

the lanthanide emissive state and the CB minimum. A temperature-dependent charge-transfer model (TDCT) provides a more realistic approach to rationalize thermal quenching via ionization to the CB, particularly over wide temperature ranges where the reduction in the magnitude of the host's bandgap must be accounted for. ^{68, 69, 94, 95} This model accounts for the energy of the phonons involved in the crossover and for the temperature dependence of the bandgap. 69, 94, 96 Accordingly, the charge transfer rate (K_{TDCT}) is given in **equations 7, 8**, and 9, where C_{TDCT} is a constant that includes the coupling factor between the two electronic states and the Stokes shift. T^* is an effective temperature that depends on the average phonon energies ($\langle \hbar \omega \rangle$). The dependence of $\Delta E_{\rm CT}$ on temperature is introduced via constants $\Delta E(0)$ and α.

$$K_{\text{TDCT}}(T) = C_{\text{TDCT}} T^{*-1/2} \exp\left(-\frac{\Delta E_{\text{CT}}}{k_B T^*}\right)$$
 (7)

$$T^* = \left(\frac{\langle \hbar \omega \rangle}{2k_B}\right) coth\left(\frac{\langle \hbar \omega \rangle}{2k_B T}\right) \tag{8}$$

$$\Delta E_{\rm CT}(T) = \Delta E(0) - \alpha T \tag{9}$$

This model has been employed to rationalize thermal quenching of 4f excited states in GdVO₄:Dy and LiNbO₃:Dy,^{69, 71} albeit at low and moderate temperatures (\leq 500 °C). Fits of MPR, CT, and TDCT models to average lifetimes $\langle \tau(T) \rangle$ are shown in **Figure 7**. We chose to use average lifetimes

to account for all components of the decay in a single metric that can be later used as a thermometric parameter. Fits were carried out using the natural logarithm of average lifetime values as a variance-stabilizing transformation (i.e., applying natural logarithm to both sides of **equation 4**). 15, 56 Absolute average temperatures were used for fits (i.e., $\langle T \rangle$ in K). The radiative rate K_R was fixed to $1/\langle \tau \rangle_{100} = 880 \text{ s}^{-1}$ in all cases, where $\langle \tau \rangle_{100}$ was the average lifetime at 100 °C. Visual inspection of **Figure 7** confirms that the onset of thermal quenching occurred between 400 and 500 °C. The MPR model was fit using $K_{\text{MPR}}(0)$ and p as adjustable parameters. ΔE_{MPR} was fixed to 8,000 cm⁻¹, a value that offered an adequate estimate of the energy difference between the center of the ${}^4I_{15/2}/{}^4F_{9/2}$ manifold and the ${}^6F_{1/2}$ state of Dy³⁺. ${}^{37, 52}$ An adequate fit was obtained (R^2 = 0.995, see Figure 7a). The resulting values for fit parameters $K_{\text{MPR}}(0)$ and p were 3.89(4.07)×10⁻¹ ³ s⁻¹ and 20.93(0.62), respectively. Both values were robust because they did not change significantly when ΔE_{MPR} was set equal to 7,300 or 8,500 cm⁻¹ (i.e., ${}^{4}F_{9/2} - {}^{6}F_{1/2}$ and ${}^{4}I_{15/2} - {}^{6}F_{1/2}$ energy gaps, respectively). The value of p was in line with those estimated for other hightemperature phosphors including YAG:Dy $(p = 20-23)^{10,52}$ and YSZ:Dy $(p = 18)^{10}$ For the latter, the reported thermal quenching temperature was also similar to BMTO:Dy (≈450 °C). The effective phonon energy derived from our fit was equal to 382 cm⁻¹ ($\Delta E_{\text{MPR}}/p$). This energy was in the lower end of the vibrational spectrum of BMTO, which features frequencies ranging from ≈100 to 900 cm⁻¹. ⁹⁷⁻¹⁰¹ Although empirical and with the same number of adjustable parameters as MPR, the CT model yielded a better fit ($R^2 = 0.998$, see Figure 7b). Comparison of both fits showed that CT provided a more accurate estimate of the onset of thermal quenching—which MPR incorrectly placed below 400 °C—and description of the slope change at ≈700 °C. Values for fit parameters C_{CT} and ΔE_{CT} were 3.97(1.47) $\times 10^{12}$ s⁻¹ and 11,230(270) cm⁻¹ (1.39 eV), respectively. The frequency factor was within the expected range of 4×10^{12} – 4×10^{13} s⁻¹.68 Lastly, the more realistic TDCT model was fit to experimental lifetimes using C_{TDCT} , $\langle \hbar \omega \rangle$, and $\Delta E(0)$ as adjustable parameters. a was fixed to 2.98 cm⁻¹ K⁻¹, a value that was extracted from a linear fit of the bathochromic shift of the maximum of the $O^{2-} \rightarrow Ta^{5+}$ charge transfer excitation band between – 195 and 505 °C (see Supporting Information, Figure S4). This value is equivalent to a decrease of ≈0.04 eV per 100 K in the charge transfer energy, in line with the bandgap narrowing expected upon increasing temperature (≈0.02–0.05 eV per 100 K).^{68, 102, 103} The TDCT model resulted in a fit identical to that provided by its CT counterpart ($R^2 = 0.998$, see Figure 7c). No differences

could be pinpointed upon visual comparison of the two fits. Values of $8.15(10.82)\times10^{12}$ s⁻¹, 464(269) cm⁻¹, and 12,675(1,377) cm⁻¹ (1.57 eV) were obtained for C_{TDCT} , $\langle\hbar\omega\rangle$, and $\Delta E(0)$, respectively. Similar to what was pointed out for MPR and CT models, values extracted for the fit parameters were physically sensible. Last but not least, it should be noted that according to the TDCT model, the energy barrier for thermal ionization of the $^4I_{15/2}$ excited state to the CB decreased from 11,787 cm⁻¹ (1.46 eV) at 25 °C to 8,583 cm⁻¹ (1.06 eV) at 1100 °C.

Results from fits of MPR and TDCT models are compiled in Figure 8. These were used to (i) estimate the position of Dy³⁺ 4f levels within the bandgap of BMTO at 25 and 1100 °C, (ii) compare the temperature dependence of nonradiative relaxation rates over the entire temperature range, and (iii) assess thermal quenching pathways. The energy level diagram at 25 °C was built by placing the CB minimum at 4.60 eV (Figure 8a), in line with experimental and theoretical estimates of the bandgap. The ⁴I_{15/2} emissive level of Dy³⁺ was placed 1.46 eV below the CB minimum according to the value of $\Delta E_{\rm CT}(298~{\rm K})$. The positions of the remaining levels of Dy³⁺ were then referred to ⁴I_{15/2}. Building the diagram at 1100 °C entailed adjusting the position of the CB minimum according to the value of $\Delta E_{\rm CT}(1373~{\rm K})$, which was equal to 1.06 eV. The position of the top of the VB was adjusted slightly upwards (≈0.03 eV) considering a decrease of 0.43 eV in bandgap over the 25-1100 °C range (vide supra). The estimated energy gaps for nonradiative relaxation via multiphonon emission and thermally activated charge transfer to the CB were comparable at 1100 °C ($\Delta E_{MPR} = 0.99 \text{ vs } \Delta E_{CT} = 1.06 \text{ eV}$). Plotting rates for these two processes as a function of temperature (Figure 8b) provides an alternative way of visualizing the two stages observed earlier in the $\langle \tau(T) \rangle$ curve. No luminescence thermal quenching was noticeable below 400 °C, where radiative relaxation dominated ($K_R > K_{MPR}, K_{TDCT}$). Quenching was clearly observable above 450 °C (T_Q), where nonradiative relaxation took over ($K_{MPR} \approx K_{TDCT} > K_R$). Calculated rates for multiphonon relaxation and thermal ionization of the 4I_{15/2} level were remarkably similar above 570 °C. When it comes to establishing which of these two was the primary pathway for nonradiative relaxation, it seems clear that luminescence thermal quenching was first driven by ionization to the CB. This conclusion stems from (i) the observation that the MPR model was unable to correctly estimate the onset of thermal quenching, and (ii) the fact that a high-order process is improbable on the lower end of the temperature range examined in this study. By contrast, we cannot be equally conclusive regarding the high temperature end. Rates for

deactivation via multiphonon emission and charge transfer to the CB were found to be nearly identical upon increasing temperature. Further, high-order multiphonon emission is known to occur at high temperatures in lanthanide(III)-doped phosphors. 10,37,52,56,59 On this basis, we cannot rule out that both quenching pathways were operational at high temperatures. Finally, we conclude by noting the potential of BMTO:Dy as a high-temperature luminescence thermometer. If used as a such, this thermosensitive phosphor would provide an operational range between \approx 450 and 1100 °C and temperature sensitivities ranging between \approx 2.1 % °C⁻¹ at 538 °C and \approx 0.9 % °C⁻¹ at 1100 °C (see Supporting Information, **Figure S5**). Although sensitivities are not typically reported for high-temperature thermosensitive phosphors, values computed herein for BMTO:Dy are comparable to those estimated for well-established materials such as Y_2O_3 :Er (1.1 % °C⁻¹ at 1100 °C), 56 $Y_3Al_5O_{12}$:Eu (1.6 % °C⁻¹ at 1100 °C), 19 and $Y_3Al_5O_{12}$:Dy (1.0 % °C⁻¹ at 1400 °C), 52

CONCLUSIONS

We investigated the response of a new high-temperature thermosensitive phosphor featuring Dy^{3+} as activator and triple perovskite $Ba_3MgTa_2O_9$ as host. Time-resolved decays of the $^4I_{15/2} \rightarrow ^6H_{15/2}$ transition of Dy^{3+} were collected between room temperature and 1100 °C. The temperature dependence of the excited state lifetime was quantitatively analyzed to establish mechanisms driving thermal quenching, which was observed above 450 °C. Two nonradiative deactivation pathways were examined: multiphonon relaxation to lower-lying 4f levels and thermally activated ionization to the host's conduction band. Fits of both models to experimental lifetimes favored the latter as the primary quenching pathway, particularly on the low temperature end of the range studied herein. At high temperatures, on the other hand, we could not rule that multiphonon relaxation was operational as an additional or alternative quenching pathway. An obvious avenue for future research would be to exploit the tunability of the perovskite host to shed further light into this particular question. Chemical substitutions that systematically impact thermal quenching via tuning of the host's electronic structure (bandgap) and vibrational spectrum (phonon energies) should help pinpoint the primary thermal quenching pathway at high temperatures.

We also evaluated the potential of Dy³⁺-doped Ba₃MgTa₂O₉ as a high-temperature optical sensor by using the temperature-dependence of the lanthanide's excited state lifetime as the thermometric parameter. The operational temperature range of the phosphor was between 450 and 1100 °C. Temperature sensitivities on the upper end of the range were comparable to those of well-

established high-temperature phosphors such as garnets. In this regard, we note that chemical substitutions mentioned above would not only be instrumental to further understanding of thermal quenching pathways but also help tuning these figures of merit.

SUPPORTING INFORMATION

The following Supporting Information is provided: (1) crystal structure and thermal analyses, (2) additional computational results, (3) intensity-threshold fits of luminescence decays, (4) variable-temperature excitation spectra, and (5) thermometric sensitivity analysis.

ACKNOWLEDGEMENTS

M.R.I. is grateful for the support of Wayne State University and the International Centre for Diffraction Data for a Thomas C. Rumble Graduate Fellowship and a Ludo Frevel Scholarship, respectively. M.R.I. and F.A.R. would like to acknowledge the financial support of the Research Corporation for Science Advancement for a Cottrell Scholar Award and of Wayne State University's Office of the Vice President for Research. Z.-F.L. acknowledges support from an NSF CAREER award (DMR-2044552). The authors are also grateful for the support of Wayne State University for the use of the X-ray diffraction core in the Lumigen Instrument Center (National Science Foundation MRI-1427926). The computational work used Bridges-2 at Pittsburgh Supercomputing Center through allocation PHY220043 from the Advanced Cyberinfrastructure Coordination Ecosystem: Services & Support (ACCESS) program, which is supported by NSF grants #2138259, #2138286, #2138307, #2137603, and #2138296. The authors thank Professors Suk Kyoung Lee and Wen Li (Department of Chemistry, Wayne State University) for providing the LabVIEW code employed for TCSPC data collection and for very helpful discussions.

REFERENCES [-, issues, 0.25" hanging, dois, Kennedy Thesis pages, 25/41 Cates/Eldridge]

- 1. Allison, S. W.; Beshears, D. L.; Cates, M. R.; Noel, B. W.; Turley, W. D., Taking an Engine's Temperature. *Mechanical Engineering* **1997**, 119, (1), 72–74.
- 2. Allison, S. W.; Gillies, G. T., Remote Thermometry with Thermographic Phosphors: Instrumentation and Applications. *Review of Scientific Instruments* **1997**, 68, (7), 2615-2650.
- 3. Khalid, A. H.; Kontis, K.; Behtash, H. Z., Phosphor Thermometry in Gas Turbines: Consideration Factors. *Proceedings of the Institution of Mechanical Engineers, Part G: Journal of Aerospace Engineering* **2010**, 224, (7), 745-755.

- 4. Brübach, J.; Pflitsch, C.; Dreizler, A.; Atakan, B., On Surface Temperature Measurements with Thermographic Phosphors: A Review. *Progress in Energy and Combustion Science* **2013**, 39, (1), 37-60.
- 5. Feist, J. P.; Heyes, A. L.; Nicholls, J. R., Phosphor Thermometry in an Electron Beam Physical Vapour Deposition Produced Thermal Barrier Coating Doped with Dysprosium. *Proceedings of the Institution of Mechanical Engineers, Part G: Journal of Aerospace Engineering* **2001**, 215, (6), 333–341.
- 6. Eldridge, J. I.; Bencic, T. J.; Allison, S. W.; Beshears, D. L., Depth-Penetrating Temperature Measurements of Thermal Barrier Coatings Incorporating Thermographic Phosphors. *Journal of Thermal Spray Technology* **2004**, 13, (1), 44–50.
- 7. Eldridge, J. I.; Wolfe, D. E., Monitoring Thermal Barrier Coating Delamination Progression by Upconversion Luminescence Imaging. *Surface and Coatings Technology* **2019**, 378, 124923.
- 8. Brübach, J.; Zetterberg, J.; Omrane, A.; Li, Z. S.; Aldén, M.; Dreizler, A., Determination of Surface Normal Temperature Gradients Using Thermographic Phosphors and Filtered Rayleigh Scattering. *Applied Physics B* **2006**, 84, (3), 537-541.
- 9. Seyfried, H.; Richter, M.; Aldén, M.; Schmidt, H., Laser-Induced Phosphorescence for Surface Thermometry in the Afterburner of an Aircraft Engine. *AIAA Journal* **2007**, 45, (12), 2966-2971.
- 10. Steenbakker, R. J. L.; Feist, J. P.; Wellman, R. G.; Nicholls, J. R., Sensor Thermal Barrier Coatings: Remote In Situ Condition Monitoring of EB–PVD Coatings at Elevated Temperatures. *Journal of Engineering for Gas Turbines and Power* **2009**, 131, 041301.
- 11. Aldén, M.; Omrane, A.; Richter, M.; Särner, G., Thermographic Phosphors for Thermometry: A Survey of Combustion Applications. *Progress in Energy and Combustion Science* **2011**, 37, (4), 422-461.
- 12. Fuhrmann, N.; Schild, M.; Bensing, D.; Kaiser, S. A.; Schulz, C.; Brübach, J.; Dreizler, A., Two-Dimensional Cycle-Resolved Exhaust Valve Temperature Measurements in an Optically Accessible Internal Combustion Engine Using Thermographic Phosphors. *Applied Physics B* **2012**, 106, (4), 945-951.
- 13. Fuhrmann, N.; Schneider, M.; Ding, C. P.; Brübach, J.; Dreizler, A., Two-Dimensional Surface Temperature Diagnostics in a Full-Metal Engine Using Thermographic Phosphors. *Measurement Science and Technology* **2013**, 24, (9), 095203.
- 14. Fuhrmann, N.; Litterscheid, C.; Ding, C. P.; Brübach, J.; Albert, B.; Dreizler, A., Cylinder Head Temperature Determination Using High-Speed Phosphor Thermometry in a Fired Internal Combustion Engine. *Applied Physics B* **2014**, 116, (2), 293-303.
- 15. Eldridge, J. I.; Allison, S. W.; Jenkins, T. P.; Gollub, S. L.; Hall, C. A.; Walker, D. G., Surface Temperature Measurements From a Stator Vane Doublet in a Turbine Afterburner Flame Using a YAG:Tm Thermographic Phosphor. *Measurement Science and Technology* **2016**, 27, (12), 125205.
- 16. Nau, P.; Yin, Z.; Lammel, O.; Meier, W., Wall Temperature Measurements in Gas Turbine Combustors With Thermographic Phosphors. *Journal of Engineering for Gas Turbines and Power* **2018**, 141, 041021.
- 17. Fouliard, Q.; Hernandez, J.; Heeg, B.; Ghosh, R.; Raghavan, S., Phosphor Thermometry Instrumentation for Synchronized Acquisition of Luminescence Lifetime Decay and Intensity on Thermal Barrier Coatings. *Measurement Science and Technology* **2020**, 31, (5), 054007.

- 18. Jenkins, T. P.; Hess, C. F.; Allison, S. W.; Eldridge, J. I., Measurements of Turbine Blade Temperature in an Operating Aero Engine Using Thermographic Phosphors. *Measurement Science and Technology* **2020**, 31, (4), 044003.
- 19. Nau, P.; Görs, S.; Arndt, C.; Witzel, B.; Endres, T., Wall Temperature Measurements in a Full-Scale Gas Turbine Combustor Test Rig With Fiber Coupled Phosphor Thermometry. *Journal of Turbomachinery* **2020**, 143, 011007.
- 20. Witkowski, D.; Rothamer, D. A., Precise Surface Temperature Measurements From 400 to 1200 K Using the Pr:YAG Phosphor. *Applied Physics B* **2021**, 127, (12), 171.
- 21. Nau, P.; Müller, A.; Petry, N.; Nilsson, S.; Endres, T.; Richter, M.; Witzel, B., Fiber-Coupled Phosphor Thermometry for Wall Temperature Measurements in a Full-Scale Hydrogen Gas Turbine Combustor. *Measurement Science and Technology* **2023**, 34, (10), 104003.
- 22. Omrane, A.; Petersson, P.; Aldén, M.; Linne, M. A., Simultaneous 2D Flow Velocity and Gas Temperature Measurements Using Thermographic Phosphors. *Applied Physics B* **2008**, 92, (1), 99-102.
- 23. Jovicic, G.; Zigan, L.; Will, S.; Leipertz, A., Phosphor Thermometry in Turbulent Hot Gas Flows Applying Dy:YAG and Dy:Er:YAG Particles. *Measurement Science and Technology* **2015**, 26, (1), 015204.
- 24. Goss, L. P.; Smith, A. A.; Post, M. E., Surface Thermometry by Laser-Induced Fluorescence. *Review of Scientific Instruments* **1989**, 60, (12), 3702-3706.
- 25. Cates, M. R.; Allison, S. W.; Jaiswal, S. L.; Beshears, D. L. *YAG:Dy and YAG:Tm Fluorescence Above 1400* °C; R03-117983; Oak Ridge National Laboratory: Oak Ridge, Tennessee, 2003; p 12.
- 26. Gentleman, M. M.; Clarke, D. R., Luminescence Sensing of Temperature in Pyrochlore Zirconate Materials for Thermal Barrier Coatings. *Surface and Coatings Technology* **2005**, 200, (5), 1264-1269.
- 27. Seyfried, H.; Särner, G.; Omrane, A.; Richter, M.; Schmidt, H.; Aldén, M. In *Optical Diagnostics for Characterization of a Full-Size Fighter-Jet Afterburner*, ASME Turbo Expo 2005: Power for Land, Sea, and Air, 2005; 2005; pp 813-819.
- 28. Chambers, M. D.; Clarke, D. R., Effect of Long Term, High Temperature Aging on Luminescence From Eu-Doped YSZ Thermal Barrier Coatings. *Surface and Coatings Technology* **2006**, 201, (7), 3942-3946.
- 29. Gentleman, M. M.; Eldridge, J. I.; Zhu, D. M.; Murphy, K. S.; Clarke, D. R., Non-Contact Sensing of TBC/BC Interface Temperature in a Thermal Gradient. *Surface and Coatings Technology* **2006**, 201, (7), 3937-3941.
- 30. Brübach, J.; Dreizler, A.; Janicka, J., Gas Compositional and Pressure Effects on Thermographic Phosphor Thermometry. *Measurement Science and Technology* **2007**, 18, (3), 764-770.
- 31. Clarke, D. R.; Gentleman, M. M., Luminescence Sensing of Temperatures in Thermal Barrier Coatings. *Surface and Coatings Technology* **2007**, 202, (4), 681-687.
- 32. Brübach, J.; Feist, J. P.; Dreizler, A., Characterization of Manganese-Activated Magnesium Fluorogermanate with Regards to Thermographic Phosphor Thermometry. *Measurement Science and Technology* **2008**, 19, (2), 025602.
- 33. Chambers, M. D.; Rousseve, P. A.; Clarke, D. R., Luminescence Thermometry for Environmental Barrier Coating Materials. *Surface and Coatings Technology* **2008**, 203, (5), 461-465.

- 34. Särner, G.; Richter, M.; Aldén, M., Investigations of Blue Emitting Phosphors for Thermometry. *Measurement Science and Technology* **2008**, 19, (12), 125304.
- 35. Chambers, M. D.; Clarke, D. R., Doped Oxides for High-Temperature Luminescence and Lifetime Thermometry. *Annual Review of Materials Research* **2009**, 39, (1), 325-359.
- 36. Chambers, M. D.; Rousseve, P. A.; Clarke, D. R., Decay Pathway and High-Temperature Luminescence of Eu³⁺ in Ca₂Gd₈Si₆O₂₆. *Journal of Luminescence* **2009**, 129, (3), 263-269.
- 37. Heyes, A. L., On the Design of Phosphors for High-Temperature Thermometry. *Journal of Luminescence* **2009**, 129, (12), 2004-2009.
- 38. Skinner, S. J.; Feist, J. P.; Brooks, I. J. E.; Seefeldt, S.; Heyes, A. L., YAG:YSZ Composites as Potential Thermographic Phosphors for High Temperature Sensor Applications. *Sensors and Actuators B: Chemical* **2009**, 136, (1), 52-59.
- 39. Fuhrmann, N.; Kissel, T.; Dreizler, A.; Brübach, J., Gd₃Ga₅O₁₂:Cr—A Phosphor for Two-Dimensional Thermometry in Internal Combustion Engines. *Measurement Science and Technology* **2011**, 22, (4), 045301.
- 40. Heeg, B.; Jenkins, T. P., Precision and Accuracy of Luminescence Lifetime-Based Phosphor Thermometry: A Case Study of Eu(III):YSZ. *AIP Conference Proceedings* **2013**, 1552, (1), 885-890.
- 41. Eldridge, J.; Bencic, T.; Zhu, D.; Allison, S.; Beshears, D.; Jenkins, T.; Howard, R. *Implementation of an Ultra-Bright Thermographic Phosphor for Gas Turbine Engine Temperature Measurements*; NASA/TM-2014-218418; Glenn Research Center: Knoxville, Tennessee, 2014.
- 42. Eldridge, J. I.; Chambers, M. D., Fiber Optic Thermometer Using Cr-Doped GdAlO₃ Broadband Emission Decay. *Measurement Science and Technology* **2015**, 26, (9), 095202.
- 43. Hashemi, A.; Vetter, A.; Jovicic, G.; Batentschuk, M.; Brabec, C. J., Temperature Measurements Using YAG: Dy and YAG: Sm Under Diode Laser Excitation (405 nm). *Measurement Science and Technology* **2015**, 26, (7), 075202.
- 44. Abou Nada, F.; Lantz, A.; Larfeldt, J.; Markocsan, N.; Aldén, M.; Richter, M., Remote Temperature Sensing on and Beneath Atmospheric Plasma Sprayed Thermal Barrier Coatings Using Thermographic Phosphors. *Surface and Coatings Technology* **2016**, 302, 359-367.
- 45. Peng, D.; Yang, L.; Cai, T.; Liu, Y.; Zhao, X.; Yao, Z., Phosphor-Doped Thermal Barrier Coatings Deposited by Air Plasma Spray for In-Depth Temperature Sensing. *Sensors* **2016**, 16, (10), 1490.
- 46. Hertle, E.; Chepyga, L.; Batentschuk, M.; Zigan, L., Influence of Codoping on the Luminescence Properties of YAG:Dy for High Temperature Phosphor Thermometry. *Journal of Luminescence* **2017**, 182, 200-207.
- 47. Yang, L.; Peng, D.; Zhao, C.; Xing, C.; Guo, F.; Yao, Z.; Liu, Y.; Zhao, X.; Xiao, P., Evaluation of the In-Depth Temperature Sensing Performance of Eu- and Dy-Doped YSZ in Air Plasma Sprayed Thermal Barrier Coatings. *Surface and Coatings Technology* **2017**, 316, 210-218.
- 48. Chepyga, L. M.; Hertle, E.; Ali, A.; Zigan, L.; Osvet, A.; Brabec, C. J.; Batentschuk, M., Synthesis and Photoluminescent Properties of the Dy³⁺ Doped YSO as a High-Temperature Thermographic Phosphor. *Journal of Luminescence* **2018**, 197, 23-30.
- 49. Eldridge, J. I., Single Fiber Temperature Probe Configuration Using Anti-Stokes Luminescence from Cr:GdAlO₃. *Measurement Science and Technology* **2018**, 29, (6), 065206.
- 50. Hertle, E.; Chepyga, L.; Batentschuk, M.; Will, S.; Zigan, L., Temperature-Dependent Luminescence Characteristics of Dy³⁺ Doped in Various Crystalline Hosts. *Journal of Luminescence* **2018**, 204, 64-74.

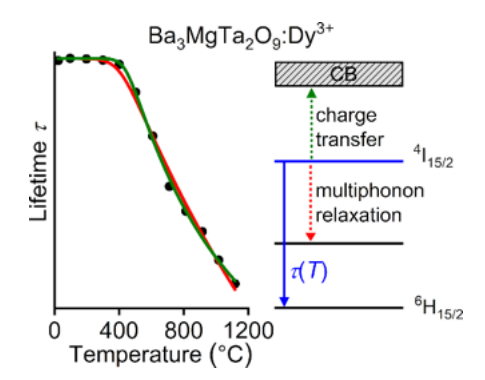
- 51. Anderson, B., R.; Livers, S.; Gunawidjaja, R.; Eilers, H., Fiber-Based Optical Thermocouples for Fast Temperature Sensing in Extreme Environments. *Optical Engineering* **2019**, 58, (9), 097105.
- 52. Allison, S. W.; Beshears, D. L.; Cates, M. R.; Scudiere, M. B.; Shaw, D. W.; Ellis, A. D., Luminescence of YAG:Dy and YAG:Dy,Er Crystals to 1700 °C. *Measurement Science and Technology* **2020**, 31, (4), 044001.
- 53. Tsuchiya, K.; Sako, K.; Ishiwada, N.; Yokomori, T., Precision Evaluation of Phosphors for the Lifetime Method in Phosphor Thermometry. *Measurement Science and Technology* **2020**, 31, (6), 065005.
- 54. Arndt, C. M.; Nau, P.; Meier, W., Characterization of Wall Temperature Distributions in a Gas Turbine Model Combustor Measured by 2D Phosphor Thermometry. *Proceedings of the Combustion Institute* **2021**, 38, (1), 1867-1875.
- 55. Feuk, H.; Nilsson, S.; Richter, M., Temperature Resolved Decay Time Components of Mg₄FGeO₆:Mn Using the Maximum Entropy Method. *Review of Scientific Instruments* **2023**, 94, (3), 034901.
- 56. Eldridge, J. I., Luminescence Decay-Based Y₂O₃:Er Phosphor Thermometry: Temperature Sensitivity Governed by Multiphonon Emission with an Effective Phonon Energy Transition. *Journal of Luminescence* **2019**, 214, 116535.
- 57. Nilsson, S.; Feuk, H.; Richter, M., High Temperature Thermographic Phosphors YAG:Tm;Li and YAG:Dy in Reduced Oxygen Environments. *Journal of Luminescence* **2023**, 256, 119645.
- 58. Kisliuk, P.; Moore, C. A., Radiation From the ${}^{4}T_{2}$ State of Cr^{3+} in Ruby and Emerald. *Physical Review* **1967**, 160, (2), 307-312.
- 59. Kennedy, J. L. Investigations of Fiber Optic Temperature Sensors Based on Yb:Y₃Al₅O₁₂. University of South Florida, 2006.
- 60. Guo, R.; Bhalla, A. S.; Cross, L. E., Ba(Mg_{1/3}Ta_{2/3})O₃ Single Crystal Fiber Grown by the Laser Heated Pedestal Growth Technique. *Journal of Applied Physics* **1994**, 75, (9), 4704-4708.
- 61. Ma, W.; Jarligo, M. O.; Mack, D. E.; Pitzer, D.; Malzbender, J.; Vaßen, R.; Stöver, D., New Generation Perovskite Thermal Barrier Coating Materials. *Journal of Thermal Spray Technology* **2008**, 17, (5), 831-837.
- 62. Jarligo, M. O.; Mack, D. E.; Vassen, R.; Stöver, D., Application of Plasma-Sprayed Complex Perovskites as Thermal Barrier Coatings. *Journal of Thermal Spray Technology* **2009**, 18, (2), 187-193.
- 63. Lufaso, M. W., Crystal Structures, Modeling, and Dielectric Property Relationships of 2:1 Ordered Ba₃MM'₂O₉ (M = Mg, Ni, Zn; M' = Nb, Ta) Perovskites. *Chemistry of Materials* **2004**, 16, (11), 2148-2156.
- 64. Youn, H.-J.; Hong, K. S.; Kim, H., Coexistence of 1:2 and 1:1 Long-Range Ordering Types in La-Modified Ba(Mg_{0.33}Ta_{0.67})O₃ Ceramics. *Journal of Materials Research* **1997**, 12, (3), 589-592.
- 65. Hoque, M. M.; Dutta, A.; Kumar, S.; Sinha, T. P., Structural and Dielectric Properties of Sr₃(MgTa₂)O₉ and Sr₃(ZnTa₂)O₉. *Physica B: Condensed Matter* **2015**, 468-469, 85-95.
- 66. Verbraeken, M. C.; Viana, H. A.; Wormald, P.; Irvine, J. T., A Structural Study of the Proton Conducting *B*-Site Ordered Perovskite Ba₃Ca_{1.18}Ta_{1.82}O_{8.73}. *Journal of Physics: Condensed Matter* **2011**, 23, (23), 234111.

- 67. Kim, Y.-I.; Woodward, P. M., Crystal Structures and Dielectric Properties of Ordered Double Perovskites Containing Mg²⁺ and Ta⁵⁺. *Journal of Solid State Chemistry* **2007**, 180, (10), 2798-2807.
- 68. Dorenbos, P., Thermal Quenching of Lanthanide Luminescence Via Charge Transfer States in Inorganic Materials. *Journal of Materials Chemistry C* **2023**, 11, (24), 8129-8145.
- 69. Nikolić, M. G.; Jovanović, D. J.; Dramićanin, M. D., Temperature Dependence of Emission and Lifetime in Eu³⁺- and Dy³⁺-Doped GdVO₄. *Applied Optics* **2013**, 52, (8), 1716-1724.
- 70. Krumpel, A. H.; van der Kolk, E.; Cavalli, E.; Boutinaud, P.; Bettinelli, M.; Dorenbos, P., Lanthanide 4*f*-Level Location in AVO₄:Ln³⁺ (A = La, Gd, Lu) Crystals. *Journal of Physics: Condensed Matter* **2009**, 21, (11), 115503.
- 71. Lisiecki, R.; Macalik, B.; Kowalski, R.; Komar, J.; Ryba-Romanowski, W., Effect of Temperature on Luminescence of LiNbO₃ Crystals Single-Doped with Sm³⁺, Tb³⁺, or Dy³⁺ Ions. *Crystals* **2020**, 10, (11), 1034.
- 72. Dhar, A.; Mansingh, A., Optical Properties of Reduced Lithium Niobate Single Crystals. *Journal of Applied Physics* **1990**, 68, (11), 5804-5809.
- 73. Toby, B. H.; Von Dreele, R. B., GSAS-II: the Genesis of a Modern Open-Source All Purpose Crystallography Software Package. *Journal of Applied Crystallography* **2013**, 46, (2), 544-549.
- 74. Rietveld, H., A Profile Refinement Method for Nuclear and Magnetic Structures. *Journal of Applied Crystallography* **1969**, 2, (2), 65-71.
- 75. Rietveld, H., Line Profiles of Neutron Powder-Diffraction Peaks for Structure Refinement. *Acta Crystallographica* **1967**, 22, (1), 151-152.
- 76. Momma, K.; Izumi, F., VESTA 3 for Three-Dimensional Visualization of Crystal, Volumetric and Morphology Data. *Journal of Applied Crystallography* **2011**, 44, (6), 1272-1276.
- 77. Kubelka, P.; Munk, F., Ein Beitrag zur Optik der Farbanstriche. Z. Technol. Phys. (Leipzig) **1931,** 12, 593–601.
- 78. Kresse, G.; Joubert, D., From Ultrasoft Pseudopotentials to the Projector Augmented-Wave Method. *Physical Review B* **1999**, 59, (3), 1758-1775.
- 79. Perdew, J. P.; Burke, K.; Ernzerhof, M., Generalized Gradient Approximation Made Simple. *Physical Review Letters* **1996**, 77, (18), 3865-3868.
- 80. Giannozzi, P.; Baroni, S.; Bonini, N.; Calandra, M.; Car, R.; Cavazzoni, C.; Ceresoli, D.; Chiarotti, G. L.; Cococcioni, M.; Dabo, I.; Dal Corso, A.; de Gironcoli, S.; Fabris, S.; Fratesi, G.; Gebauer, R.; Gerstmann, U.; Gougoussis, C.; Kokalj, A.; Lazzeri, M.; Martin-Samos, L.; Marzari, N.; Mauri, F.; Mazzarello, R.; Paolini, S.; Pasquarello, A.; Paulatto, L.; Sbraccia, C.; Scandolo, S.; Sclauzero, G.; Seitsonen, A. P.; Smogunov, A.; Umari, P.; Wentzcovitch, R. M., QUANTUM ESPRESSO: A Modular and Open-Source Software Project for Quantum Simulations of Materials. *Journal of Physics: Condensed Matter* **2009**, 21, (39), 395502.
- 81. Heyd, J.; Scuseria, G. E.; Ernzerhof, M., Hybrid Functionals Based on a Screened Coulomb Potential. *The Journal of Chemical Physics* **2003**, 118, (18), 8207-8215.
- 82. Wang, C.; Cui, R.; Zhang, J.; Deng, C., Synthesis and Characterization of Ba₃MgTa₂O₉:xSm³⁺ Orange-Red Phosphor with Excellent Color Purity and Superior Color Stability. *Inorganic Chemistry Communications* **2023**, 155, 111065.
- 83. Kang, Z. H.; Guo, R. Z.; Da Shi, R.; Zhu, X. L.; Chen, X. M., Co-Optimization of Microwave Dielectric Properties in Ba(Mg_{1/3}Ta_{2/3})O₃ Complex Perovskite Ceramics Through Ordered Domain Engineering. *Journal of the American Ceramic Society* **2023**, 106, (6), 3471-3480.

- 84. Takahashi, A.; Kumagai, Y.; Miyamoto, J.; Mochizuki, Y.; Oba, F., Machine Learning Models for Predicting the Dielectric Constants of Oxides Based on High-Throughput First-Principles Calculations. *Physical Review Materials* **2020**, 4, (10), 103801.
- 85. Borlido, P.; Doumont, J.; Tran, F.; Marques, M. A. L.; Botti, S., Validation of Pseudopotential Calculations for the Electronic Band Gap of Solids. *Journal of Chemical Theory and Computation* **2020**, 16, (6), 3620-3627.
- 86. Wang, C.; Cui, R.; Zhang, J.; Tai, Y.; Zhao, T.; Zhang, B.; Deng, C., A Novel Orange-Red Ba₃MgTa₂O₉:Eu³⁺ Phosphor Synthesis and Luminescence Properties in WLEDs. *Optical Materials* **2023**, 140, 113891.
- 87. Partlow, W. D.; Moos, H. W., Multiphonon Relaxation in LaCl₃:Nd³⁺. *Physical Review* **1967**, 157, (2), 252-256.
- 88. Riseberg, L. A.; Gandrud, W. B.; Moos, H. W., Multiphonon Relaxation of Near-Infrared Excited States of LaCl₃:Dy³⁺. *Physical Review* **1967**, 159, (2), 262-266.
- 89. Weber, M. J., Radiative and Multiphonon Relaxation of Rare-Earth Ions in Y₂O₃. *Physical Review* **1968**, 171, (2), 283-291.
- 90. Riseberg, L. A.; Moos, H. W., Multiphonon Orbit-Lattice Relaxation of Excited States of Rare-Earth Ions in Crystals. *Physical Review* **1968**, 174, (2), 429-438.
- 91. Seitz, F., Interpretation of the Properties of Alkali Halide-Thallium Phosphors. *The Journal of Chemical Physics* **1938**, 6, (3), 150-162.
- 92. Mott, N. F., On the Absorption of Light by Crystals. *Proceedings of the Royal Society of London. Series A. Mathematical and Physical Sciences* **1938**, 167, (930), 384-391.
- 93. Fonger, W. H.; Struck, C. W., Eu^{+3 5}D Resonance Quenching to the Charge-Transfer States in Y₂O₂S, La₂O₂S, and LaOCl. *The Journal of Chemical Physics* **1970**, 52, (12), 6364-6372.
- 94. Struck, C. W.; Fonger, W. H., Quantum-Mechanical Treatment of Eu⁺³ $4f\rightarrow 4f$ and $4f\rightarrow$ Charge-Transfer-State Transitions in Y₂O₂S and La₂O₂S. *The Journal of Chemical Physics* **1976**, 64, (4), 1784-1790.
- 95. Dorenbos, P., Effect of Temperature on Lanthanide Charge Transition Levels and Vacuum Referred Binding Energies. *Journal of Luminescence* **2024**, 269, 120443.
- 96. Englman, R.; Jortner, J., The Energy Gap Law for Radiationless Transitions in Large Molecules. *Molecular Physics* **1970**, 18, (2), 145-164.
- 97. Siny, I. G.; Tao, R.; Katiyar, R. S.; Guo, R.; Bhalla, A. S., Raman Spectroscopy of Mg–Ta Order–Disorder in BaMg_{1/3}Ta_{2/3}O₃. *Journal of Physics and Chemistry of Solids* **1998**, 59, (2), 181-195.
- 98. Chia, C.-T.; Chen, Y.-C.; Cheng, H.-F.; Lin, I.-N., Correlation of Microwave Dielectric Properties and Normal Vibration Modes of *x*Ba(Mg_{1/3}Ta_{2/3})O₃–(1–*x*)Ba(Mg_{1/3}Nb_{2/3})O₃ Ceramics: I. Raman Spectroscopy. *Journal of Applied Physics* **2003**, 94, (5), 3360-3364.
- 99. Chen, Y.-C.; Cheng, H.-F.; Liu, H.-L.; Chia, C.-T.; Lin, I.-N., Correlation of Microwave Dielectric Properties and Normal Vibration Modes of *x*Ba(Mg_{1/3}Ta_{2/3})O₃–(1–*x*)Ba(Mg_{1/3}Nb_{2/3})O₃ Ceramics: II. Infrared Spectroscopy. *Journal of Applied Physics* **2003**, 94, (5), 3365-3370.
- 100. Wang, C.-H.; Jing, X.-P.; Wang, L.; Lu, J., XRD and Raman Studies on the Ordering/Disordering of Ba(Mg_{1/3}Ta_{2/3})O₃. *Journal of the American Ceramic Society* **2009**, 92, (7), 1547-1551.
- 101. Yadong, D.; Guanghui, Z.; Liling, G.; Hanxing, L., First-Principles Study of the Difference in Permittivity Between Ba(Mg_{1/3}Ta_{2/3})O₃ and Ba(Mg_{1/3}Nb_{2/3})O₃. *Solid State Communications* **2009**, 149, (19), 791-794.

- 102. Pässler, R., Moderate Phonon Dispersion Shown by the Temperature Dependence of Fundamental Band Gaps of Various Elemental and Binary Semiconductors Including Wide-Band Gap Materials. *Journal of Applied Physics* **2000**, 88, (5), 2570-2577.
- 103. Pässler, R., Temperature Dependence of Fundamental Band Gaps in Group IV, III–V, and II–VI Materials Via a Two-Oscillator Model. *Journal of Applied Physics* **2001**, 89, (11), 6235-6240.

TABLE OF CONTENTS



The luminescence response of Dy³⁺-doped Ba₃MgTa₂O₉ (BMTO:Dy) between room temperature and 1100 °C was studied in the context of high-temperature thermosensitive phosphors.